

Microfluidic mixing via transverse electrokinetic effects in a planar microchannel

N. Scott Lynn · Charles S. Henry · David S. Dandy

Received: 6 November 2007 / Accepted: 13 January 2008 / Published online: 12 February 2008
© Springer-Verlag 2008

Abstract A new micromixer incorporating integrated electrodes deposited on the bottom surface of a glass/PDMS microchannel is used to induce a localized, perpendicular electric field within pressure driven axial flow. The presence of the electric field drives electro-osmotic flow in the transverse direction along the channel walls, creating helical motion that serves to mix the fluid. A numerical model is used to describe the three-dimensional flow field, where characterization is performed via particle tracking of passive tracer particles, and the conditional entropy (S_{lc}) is utilized to approximate the extent of mixing along cross-sectional planes. The geometrical parameters and operating conditions of the numerical model are used to fabricate an experimental device, and fluorescence microscopy measurements are used to verify mixing of rhodamine B across the width of the microchannel for a wide range of fluid flow rates. The results demonstrate that under certain operating conditions and selective placement of the electrode gaps along the width of the microchannel, efficient mixing can be achieved within 6 mm of the inlet.

Keywords Micro-mixing · Electro-osmosis · Integrated electrodes · PDMS

List of symbols

L_{mix} characteristic length for mixing
 T_{mix} characteristic time for mixing

N. S. Lynn · D. S. Dandy (✉)
Department of Chemical and Biological Engineering,
Colorado State University, Fort Collins, CO 80523, USA
e-mail: dandy@colostate.edu

C. S. Henry
Department of Chemistry, Colorado State University,
Fort Collins, CO 80523, USA

ϕ externally applied potential
 λ_d debye length
 ε dielectric constant of the fluid
 ε_o permittivity of vacuum
 ζ zeta-potential
 \vec{E} electric field vector
 p pressure
 μ viscosity
 \vec{u} linear velocity
 φ stream function
 l_e axial length of the electrode
 w_g width of the electrode gap
 w_c center position of the electrode gap
 t_{comp} computational time for particle advection
 t_n average computational time for advection between planes
 S_{lc} conditional mixing entropy
 p_j probability that a particle is in bin j irrespective of species
 $p_{c,j}$ probability that a particle is of the type c whose position is in bin j
 δ_a adjusted extent of mixing
 I_i fluorescent intensity at pixel i during active mixing
 $I_{i,o}$ fluorescent intensity at pixel i if no active mixing occurs
 N total number of pixels across the width of the micro-channel
 w width of micro-channel
 h height of micro-channel
 n total number of electrode cycles
 F mixing effectiveness
 M number of bins used to discretize channel cross-sections
 w_b width of bin
 l_i axial position at the start of the i -th electrode cycle

1 Introduction

In recent years there has been a remarkable growth in research directed toward analytical devices on the micron scale. Lab-on-a-chip technology has the promise to fully integrate all stages of an analytical process, including chemical synthesis, characterization, separation, and detection within the confines of several square centimeter area (Stone et al. 2004). As in their macroscale counterparts, fluid mixing becomes a very important, albeit inherently difficult step on the microscale. The small characteristic length scale w , along with a limited range of obtainable average linear fluid velocities u , dictate that the Reynolds number ($Re = uw/\nu$) for a fluid with kinematic viscosity ν is constrained to values below 100. At these Reynolds numbers, fluid flow is well within the laminar regime, and without intervention, mixing relies principally on molecular diffusion. In a continuous flow device, the characteristic length needed for complete mixing of two fluid streams is on the order of $L_{\text{mix}} = t_{\text{mix}} \cdot u = w^2 u / D = Pe \cdot w$, where Pe is the mass transfer Peclet number. Consequently, mixing of fluids with low molecular diffusivities D can require channel lengths on the order of tens of centimeters, too long for many lab-on-a-chip applications. One of the most effective methods to enhance diffusive mixing within a microchannel is to generate non-axial flow within the microchannel, stirring the fluid in a manner such that analyte concentration gradients will be increased within the channel, thus effectively decreasing the diffusion distance required for mixing.

Microfluidic mixing can be accomplished in an active or passive manner. Passive micromixers rely on the existing geometry of the microchannel to perturb a laminar flow field away from straight streamlines. The simplest conceptual design of a passive type micromixer is the lamination mixer. This mixer systematically splits and re-layers a fluid stream to geometrically increase the solute concentration gradients within the channel, and has been experimentally realized by several groups (Therriault et al. 2003; Chen and Meiners 2004; Neils et al. 2004; Cha et al. 2006). The lamination type mixer employs 3D geometries involving complicated, multiplanar microfabrication strategies, which are difficult to fabricate via standard soft lithographic methods (Xia and Whitesides 1998). Another type of passive mixing design is the rotational-type mixer, where non-axial flows are used in an attempt to efficiently stir the fluid cross-section of a microchannel. Several groups have investigated the use of spiral microchannels to promote fluid mixing (Jiang et al. 2004; Schonfeld and Hardt 2004; Yamaguchi et al. 2004a, b; Yang et al. 2005; Sudarsan and Ugaz 2006), where non-axial flow is generated from the naturally occurring Dean vortices. Efficient mixing can also be promoted by the use of oblique grooves

on a channel surface, first demonstrated in the slanted groove micromixer (SGM) (Stroock et al. 2002a) and staggered herringbone mixer (SHM) (Stroock et al. 2002b). The SGM has since been extended to include geometrical barriers in the center of the channel (Kim et al. 2004), and oblique grooves on the sidewall of the channel in addition to those on the floor (Sato et al. 2005).

Unlike passive micromixers, active micromixers utilize external forces, such as electrokinetic and applied pressure forces, to achieve mixing. Active mixers have employed magnetic beads (Suzuki et al. 2004), peristaltic wall movement (Selverov and Stone 2001), and magnetohydrodynamic actuation (West et al. 2003) as external forces. A well known example of active micromixing involves subjecting a continuous flow microchannel to multiple, pressure-driven, periodic, closed cross-channel currents (Niu and Lee et al. 2003; Dodge et al. 2004; Niu et al. 2006). External mechanical methods are then used to control the frequency and amplitude of the cross-channel currents.

Electrokinetic phenomena have been widely used in microfluidic mixing (Chang and Yang 2007). Several studies have utilized ac electric fields to promote an electrokinetic instability (EKI) within a microchannel (Oddy et al. 2001; Lin et al. 2004; Sundaram and Tafti 2004; Park et al. 2005). Similarly, liquids exposed to transverse electrohydrodynamic (EHD) forces have been used to promote a mixing environment (Leu and Ma 2005). In EKI and EHD, the use of high-voltage electric fields requires large, high-voltage power supply equipment. Electro-osmotic flow (EOF) is used to create mixing via non-axial flow generation in channels with oblique grooves (Johnson and Locascio 2002) and heterogeneous channel surface charges, created by either active (Lee et al. 2004; Lin et al. 2005; Wu and Liu 2005) or passive methods (Biddiss et al. 2004; Chang and Yang 2004, 2006). The use of EOF to mix fluids generally relies on an applied potential drop over the entire channel length, where fields of necessary strength require large potentials (>1 kV), again requiring high-voltage power supplies.

To reduce the electric potential drop needed for relevant EOF flow magnitudes, integrated metal electrodes may be fabricated such that the distance between electrodes is on the order of the size of the microchannel. Electro-osmotic manipulation of fluids using integrated electrodes has recently been used for several applications. McKnight et al. used pairs of integrated electrodes to pump fluids in an open microfluidic device, in which EOF was demonstrated between an electrode gap as small as 60 μm (McKnight et al. 2001). Lammertink et al. used integrated electrodes to mix nanoliter volumes via recirculation in a closed microchannel (Lammertink et al. 2004). These two studies worked on the principal of an electric field applied parallel

to the microfluidic channel axis, thus inducing EOF in the axial direction. Gitlin et al. fabricated an electro-osmotic micropump using a pair of integrated electrodes situated below a microchannel with oblique grooves on the ceiling (Gitlin et al. 2003). Transverse EOF was observed between the electrodes, where the resulting recirculation across the anisotropic grooves served to pump fluid axially through the microchannel.

Transverse EOF can be efficiently utilized for microfluidic mixing strategies. Qian et al. first theorized an electro-osmotic stirrer in a two-dimensional cavity with heterogeneous surface charges on the cavity walls (Qian and Bau 2002, 2005); however, it was not reported how the electric field was created, or possible three-dimensional implementations of such device. Pacheco et al. later theorized that efficient mixing could be achieved in three-dimensional channels by subjecting pressure driven flow to a transverse moving wall condition on the top and bottom microchannel walls (Pacheco et al. 2006). The moving wall condition, created by a transverse electric field, could be controlled via multiple electrodes built into the channel sidewalls. Although efficient in design, this type of device presents several difficulties, as fabrication of multiple electrodes on the channel sidewalls can be not only difficult, but also costly and time intensive. Until now, no mixer of this type has been experimentally realized.

Rather than place the integrated electrodes along the channel sidewalls, it is straightforward to use standard micro-fabrication processes to place integrated electrodes along the channel floor. In the present work a new method is described for achieving microfluidic mixing through application of a localized electric field perpendicular to the mean flow direction driven by a pressure gradient in a planar microchannel (Fig. 1). Integrated electrodes are fabricated such that there exists a small gap situated perpendicular to the channel axis. A potential drop across the gap drives EOF perpendicular to the primary flow direction, thereby creating several non-axial recirculation flow profiles. The three-dimensional velocity field of such a

device may be described by a numerical model, and the resulting mixing characteristics may be approximated with the use of particle tracking of passive tracers. The numerical results show that, through control of the electrode geometry-gap width, gap location, axial separation, and applied potential, it is possible to induce rapid micro-mixing in short axial distances. Furthermore, this study details the operation of an experimental mixer, fabricated via standard micro-fabrication methods, which displays the same trends as predicted by the numerical model for the same geometry and operating parameters.

2 Methods

2.1 Governing equations

Electro-osmotic flows in microchannels are generally restricted to small Reynolds numbers; neglecting the inertial and time dependent terms in the Navier-Stokes equations, the cross-sectional flow field is modeled with the pseudo steady-state Stokes equation, along with the incompressible continuity equation:

$$-\nabla p + \mu \nabla^2 \vec{u} = 0 \tag{1}$$

$$\nabla \cdot \vec{u} = 0. \tag{2}$$

Equations (1) and (2) are solved as follows: two dimensional creeping flow of a viscous incompressible fluid can be described by the stream function, whose solution obeys the biharmonic equation (Meleshko 1998)

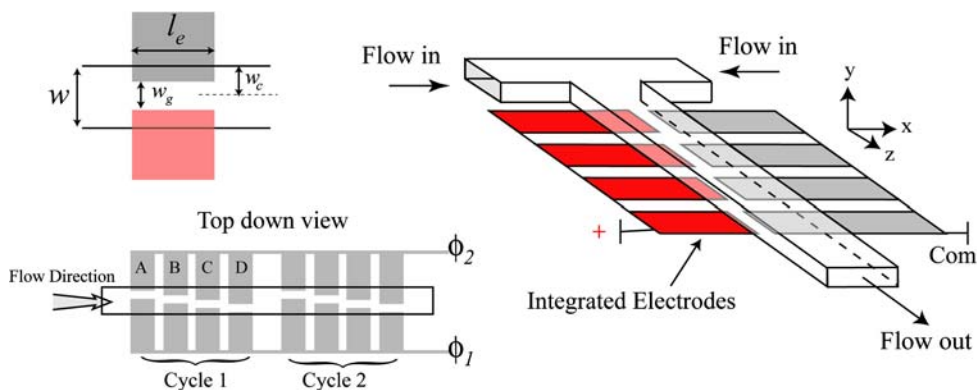
$$\nabla^4 \phi = 0. \tag{3}$$

The velocity field is obtained from ϕ via

$$u_x = \frac{\partial \phi}{\partial y}, \quad u_y = -\frac{\partial \phi}{\partial x}, \tag{4}$$

with impermeable boundary conditions $\phi_e = \text{constant}$ on the electrode bearing surfaces. EOF on non-electrode surfaces is estimated using the Helmholtz-Smoluchowski equation (Anderson 1989) along the top and bottom walls,

Fig. 1 Schematic of the micro-mixing device used within this study, along with the geometric parameters and overall electrode cycle layout



$$\frac{\partial \phi_w}{\partial y} = u_{\text{EOF},x} = -\frac{\varepsilon_o \varepsilon \zeta}{\mu} E_x, \quad (5)$$

and the channel sidewalls,

$$\frac{\partial \phi_w}{\partial x} = -u_{\text{EOF},y} = \frac{\varepsilon_o \varepsilon \zeta}{\mu} E_y, \quad (6)$$

where μ is the viscosity of the electrolyte solution, ε is the dielectric constant of the liquid, ε_o is the permittivity of vacuum, and ζ is the zeta-potential of the surface. E_x and E_y are the x and y components of the electric field vector, \vec{E} , respectively. The electric field \vec{E} is found via

$$\vec{E} = -\nabla \phi, \quad (7)$$

where ϕ is the externally applied potential distribution. According to electrostatics theory (Hunter 1981), the externally applied potential distribution in a cavity is governed by the Laplace equation

$$\nabla^2 \phi = 0. \quad (8)$$

The boundary conditions for Eq. (8) are

$$\phi_e = \phi_{\text{applied}}, \quad \frac{\partial \phi_w}{\partial \hat{n}} = 0, \quad (9)$$

where the subscripts e and w represent electrode and wall surfaces.

2.2 Numerical approach

Figure 1 displays the structure of the electro-osmotic micromixer. The axial length of the electrode is denoted as l_e , and the width and center position of the electrode gap are w_g and w_c , respectively. For externally driven flow rates of water-based electrolytes corresponding to an average linear velocity $\langle u_z \rangle < 5 \text{ mm s}^{-1}$ through a microchannel of width $w = 100 \text{ }\mu\text{m}$, the Reynolds number ($Re = \langle u_z \rangle w / \nu$) will be on the order of $Re < 0.5$. If the axial length of the individual electrodes is considerably larger than the width of the microchannel, the potential distribution along the axial direction within the individual electrodes may be assumed constant. Thus, if the spacing between the individual electrodes is considerably larger than w_g , we can neglect inter-electrode potential distributions and edge effects, and the three-dimensional velocity field can be well approximated as a superposition of the velocity field given by Eq. (4) and the axial velocity field, $\vec{u}_z(x,y)$, acquired from the Boussinesq series solution for flow in a rectangular duct.

A numerical approach is implemented to solve the governing Eqs. (3) and (8) along with the corresponding boundary conditions (5), (6), and (9). Equation (8) was discretized with a second-order accurate finite difference scheme and solved via a successive over-relaxation (SOR)

method, where the typical distance between nodes was $0.5 \text{ }\mu\text{m}$, which was predetermined (data not shown) such that the predicted flow field was independent of the mesh density. The convergence requirements for the normalized residuals concerning ϕ was 10^{-12} . The electric field is then found via Eq. (7), and used as a boundary condition in Eqs. (5) and (6). Equations (3) and (4) are solved simultaneously via a fourth-order accurate SOR scheme as discussed in Altas et al. (Altas et al. 1998), where the convergence requirements for the normalized residuals for φ was 10^{-15} . The numerical methods in this study were verified with the two-dimensional quasi-analytic flow profiles for the electrode geometries displayed by Qian et al. (Qian and Bau 2002, 2005).

2.3 Mixer characterization

To characterize the mixing efficiency of the three-dimensional flow field, non-interacting, mass less tracer particles are injected into the mixer and their motion tracked in space and time. The passive tracers do not affect the flow field, and are considered diffusionless. The positions of the tracers are calculated as a function of time via integration of the three-dimensional velocity field:

$$\vec{x}(t) = \vec{x}(t_o) + \int_{t_o}^t \vec{u}(x,y,z) dt, \quad (10)$$

where integration is carried out with a fourth-order Runge-Kutta scheme with a constant time step of $\Delta t = 0.001$ seconds. Because there exist problematic artifacts when advecting passive tracers forward in time, a backtrace method similar to Stone et al. (Stone and Stone 2005) is employed for both imaging of downstream tracer distributions and mixing characterization. The backtrace method involves initializing an ordered set of tracer particles on a cross sectional plane of interest ($z > 0$), and advecting each particle backward in time until the inlet plane ($z = 0$) is reached. Each tracer particle is then allocated a color (red, blue) based on the tracer position on the inlet plane. The initialization of the tracers at the mixer outlet is performed such that the distance between neighboring particles is constant, which allows for very fine resolution concerning the distribution of tracers and avoids the introduction of large gaps between tracers. In this study, the microchannel inlet is separated into two vertical regions, designating red or blue tracers, respectively, such that the tracer flow resembles perfectly segregated tracer distribution at the channel inlet. The main drawback to the backtrace method is its intensive computational nature, as the time required for analysis of n evenly spaced cross-sectional planes scales as

$$t_{\text{comp}} = \sum_{i=1}^n nt_n, \tag{11}$$

where t_n is the average computational time required to advect particles between neighboring planes (as opposed to $t_{\text{comp}} = nt_n$ for forward advection).

Despite the extensive body of literature focused on the numerical characterization of mixing processes at the micro- and macro-scales using massless tracer particles, there is not unanimous consensus regarding the best method to calculate the extent of mixing of the dispersed particles in time or space. In this study, the extent of mixing within a distribution of tracer particles is characterized using the entropic methods of Camesasca et al. which has been previously shown to be successful in the characterization of several mixing processes (Camesasca et al. 2005, 2006). In this method, the downstream x,y cross-sectional planes are divided into M equally sized spatial bins, and the conditional entropy S_{ic} is averaged over all bins as

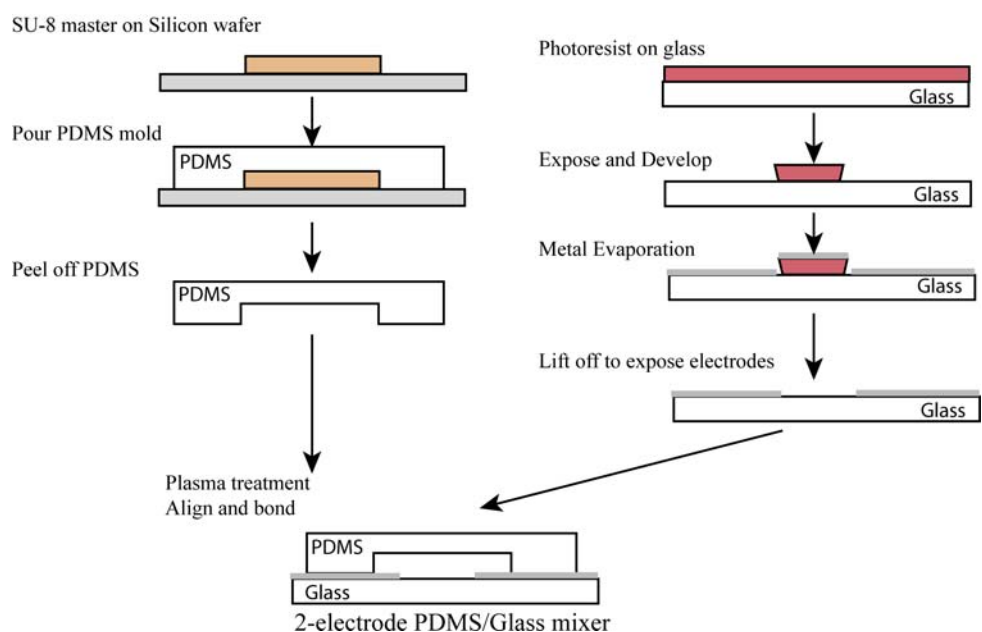
$$S_{ic} = -\frac{1}{\ln(2)} \sum_{j=1}^M p_j \sum_{c=1}^C p_{c,j} \ln p_{c,j}, \tag{12}$$

where p_j is the probability that a particle is in bin j irrespective of species, and $p_{c,j}$ is the probability that a particle is of the type c whose position is in bin j . For this study, two particle species are employed (red and blue). The conditional entropy S_{ic} is thus normalized by $\ln(2)$, as in Camesasca et al. whereby a value of $S_{ic} = 0$ indicates that no mixing has occurred between the two species, and a value of $S_{ic} = 1$ indicates a well mixed solution on the scale of the typical size of the bin.

2.4 Experimental methods

Fabrication of the mixers was performed with a soft lithographic method using poly(dimethylsiloxane) (PDMS, Sylgard 184, Dow Corning) for the channel top and sidewalls, sealed to a glass bottom containing patterned, integrated thin film electrodes. The fabrication process may be viewed in Fig. 2. The PDMS microchannels were cured over a raised Su-8 master developed onto a silicon wafer and subsequently subjected to a PDMS oligomer extraction process similar to Lee et al. (Lee et al. 2003), which has been shown to stabilize the hydrophilic nature of oxidized PDMS for up to 7 days (Vickers et al. 2006). To prepare the electrodes, a bi-layer photoresist stack (Microchem LOR 10B, Shipley 1818) was spun onto a cleaned, dehydrated glass slide. Following UV exposure and development to expose the electrode sites, 30 nm of Au was deposited onto a 6 nm Ti adhesion layer using e-beam evaporation. After lift-off of the metal layer, holes were drilled into the glass slide to provide fluid access to the mixer through the use of Nanoport fittings (Upchurch). The glass slide and PDMS layer were then cleaned and exposed to O_2 plasma (25 W, 370 mTorr) to strengthen the PDMS/glass irreversible bond and minimize the contact angle between PDMS and water (Bhattacharya et al. 2005). The two layers were then aligned and irreversibly bonded. Syringe pumps were used to deliver buffer solutions of 5 mM TES (*N*-[tris-hydroxymethyl]methyl-2-aminoethanesulfonic acid, Sigma), pH = 7.5, to both channel inlets, where one inlet contained 0.1 mM rhodamine B (Sigma) for mixing analysis. Exposed bonding pads on the periphery of the glass slide were used to connect the integrated electrodes to a power supply (HP 6217A) via patch clips.

Fig. 2 Fabrication process used to create the glass/PDMS mixer. The PDMS mold constitutes the channel top and sidewalls. The channel bottom is composed of the metal electrodes on a glass substrate



2.5 Imaging acquisition

Fluid micromixing was monitored by fluorescence of rhodamine B using two-dimensional images captured by an inverted microscope equipped with an epifluorescence attachment (Nikon TE-2000U) and fitted with a CCD camera (Coolsnap fx). Fluorescence intensity images of the unmixed and mixed states were acquired at a fixed distance from the T-junction. To quantify the mixing performance, an adjusted extent of mixing (δ_a) is introduced as

$$\delta_a = 1 - \sqrt{\frac{\sum_{i=1}^N (I_i - \langle I_i \rangle)^2}{\sum_{i=1}^N (I_{i,o} - \langle I_{i,o} \rangle)^2}}, \quad (13)$$

where I_i is the intensity at pixel i during active mixing, $I_{i,o}$ is the intensity at pixel i if no active mixing occurs ($\Delta\phi = 0$), and N is the total number of pixels across the width of the microchannel. The fluid passing through the xy -plane downstream of any integrated electrode has undergone a limited amount of diffusive mixing (no active mixing), thus the standard extent of mixing is adjusted to this unmixed state rather than the state corresponding to the plane at $z = 0$ (T-junction). The adjusted extent of mixing is defined such that $\delta_a = 1$ for well-mixed solutions (or solutions which display constant fluorescence intensity across the width of the micro-channel), whereas $\delta_a = 0$ for solutions which display no change from the unmixed state. The method of top down fluorescence analysis, although limited in the case of horizontally laminated fluorescent streams, has been previously used with success to characterize micro-mixing devices (Oddy et al. 2001; Johnson and Locascio 2002; Biddiss et al. 2004).

3 Numerical results

3.1 Two-dimensional flow profiles

It is convenient to use Eq. (3) to calculate the flow field because the contours of the stream function naturally represent the fluid streamlines in the domain of interest. Figure 3 displays the potential distributions and fluid

streamlines for several electrode arrangements in a two-dimensional microcavity. All simulations within this study pertain to a micro-cavity with dimensions $w = 140 \mu\text{m}$ and $h = 60 \mu\text{m}$. The electrode arrangements in Fig. 3 correspond to an electrode gap of $w_g = 50 \mu\text{m}$, where the position of the gap was systematically staggered along the width of the microchannel. The ζ -potential of the cavity floor was assumed to be $\zeta = -0.05 \text{ V}$, whereas the top and sidewalls are $\zeta = -0.08 \text{ V}$, consistent with the values associated with the glass floor and PDMS cap (Sze et al. 2003). In each of the electrode geometries shown in Fig. 3, there exists a primary recirculation region directly above the electrode gap, and a weaker, secondary, counter-rotating recirculation region in the remaining cavity domain. Because the electric field magnitude within the gap ($E \approx \Delta\phi/w_g$) is much larger than along the channel sidewalls ($E \approx \Delta\phi/(2h + w)$), fluid velocities are much higher within the primary recirculation regions.

3.2 Three-dimensional model

The three-dimensional velocity field of a mixing device shown in Fig. 1 can be described as follows:

$$\vec{u}(x, y, z) = \vec{u}_z(x, y) + \vec{u}_n(x, y), \quad (14)$$

where $\vec{u}_z(x, y)$ is obtained from a Boussinesq series solution, and the non-axial components $\vec{u}_n = \vec{u}_x + \vec{u}_y$ are obtained from the solution to Eq. (4) for an electrode cycle determined by the flow fields shown in Fig. 3 and assembled as:

$$\vec{u}_n(x, y) = \begin{cases} \vec{u}_A & l_i < z < l_i + l_e \\ \vec{u}_B & l_i + l_e < z < l_i + 2l_e \\ \vec{u}_C & l_i + 2l_e < z < l_i + 3l_e \\ \vec{u}_D & l_i + 3l_e < z < l_i + 4l_e \end{cases} \quad (15)$$

where l_i is the axial position of the start of the i -th electrode cycle. Eq. (15) describes a mixer with an overall electrode cycle pattern $[\text{ABCD}]_n$, where n is the total number of electrode cycles within the mixer, and inter-electrode flow is neglected. This study involves the comparison of the four electrode cycle pattern $[\text{ABCD}]_n$ and the two electrode cycle pattern $[\text{BC}]_n$.

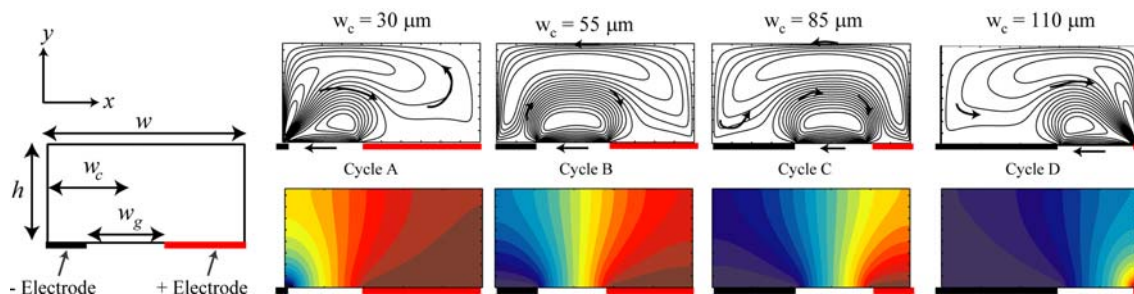


Fig. 3 Two-dimensional streamlines and ϕ contour plots corresponding to the four electrode geometries considered in this study

Figure 4 displays the distribution of 100,000 tracers corresponding to x,y -planes situated at the end the first eight electrodes for a mixer with an overall electrode cycle pattern of $[ABCD]_2$. The bulk flow rates for the two cases correspond to $\langle u_z \rangle = 0.4 \text{ mm s}^{-1}$ for Fig. 4a, and $\langle u_z \rangle = 1.6 \text{ mm s}^{-1}$ for Fig. 4b. The red and blue tracers were initially segregated in equal proportions to the right and left sides of the microchannel inlet, respectively. The applied potential drop between the electrodes is $\Delta\phi = 2.0 \text{ V}$, and the length and dimension of each electrode gap is $l_e = 500 \text{ }\mu\text{m}$ and $w_g = 50 \text{ }\mu\text{m}$, where the associated values of w_c are given in Fig. 3.

Although small amounts of mixing occur for each individual electrode, the combined effect of the two mixing cycles is quite dramatic. For Fig. 4a, the channel cross-section appears visually well mixed at the outlet, positioned 4 mm downstream of the inlet. As expected, as the bulk flow rate increases, the magnitude of stirring over each electrode decreases, which is visually apparent in the figures. However, even though the channel cross-section at the outlet of Fig. 4b maintains a large level of heterogeneity, it may be concluded that only several more electrode cycles will be needed to achieve the level of mixing seen in the outlet of Fig. 4a. It should be noted that, because the backtrace method is employed to generate the tracer distributions shown in Fig. 4, the ratio of red to blue tracers does not remain constant as the tracers pass through x,y -planes of interest. However, this has a negligible effect on the conditional entropy of the tracer distribution in each x,y plane.

3.3 Mixing mechanism

The tracer distributions shown in Fig. 4 are important in qualitatively determining both where good mixing is

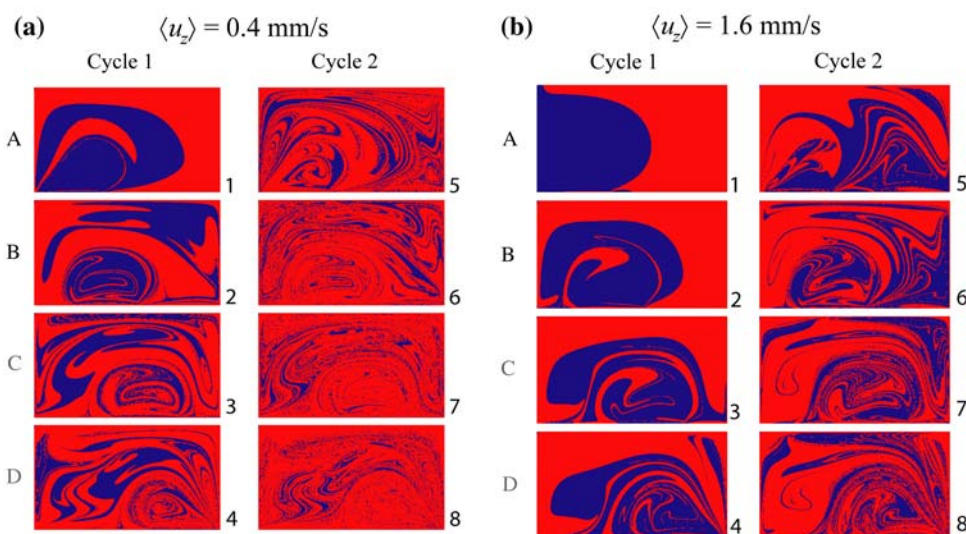
occurring within x,y -planes and potential regions of invariance within overall electrode cycle patterns. It may be concluded from Fig. 4 that the overall mixing mechanism is composed of two parts:

Rapid mixing within the primary recirculation Lamination of fluid occurs very rapidly within the primary recirculation region situated directly above the electrode gaps associated with the four electrode cycles shown in Fig. 3. The fluid is simultaneously stretched and folded within this region. Fluid breakup occurs as the electrode gap is staggered along the width of the mixer along periodic axial lengths. Because the primary recirculation occupies a region constrained to the lower part of the channel, only fluid within this region is subject to rapid mixing.

Non-axial transport within the secondary recirculation The secondary recirculation region serves to transport fluid in opposite directions along the top and sidewalls of the channel. Due to the smaller magnitudes of non-axial velocity, little lamination occurs within this region. Thus it appears the benefit of this secondary recirculation is to transport regions of fluid to the lower half of the channel. As regions of fluid reach the lower parts of the channel there exists the probability that it will be entrained in a primary recirculation region upon entering a new electrode cycle.

It has been demonstrated here that an applied potential across a staggered electrode gap has the potential to rapidly mix fluids within short axial distances. Equation (12) can be used to quantify the extent of mixing in the x,y -planes located at the end of each individual electrode. The conditions associated with in Fig. 4 lead to a quantitatively well mixed solution within 4 mm of the inlet, as the conditional entropy at the eighth electrode is calculated as $S_{1c} = 0.95$ (1,000 bins) for case (a) whereas a value of $S_{1c} = 0.75$ (1,000 bins) is calculated for case (b).

Fig. 4 Tracer distributions (100,000 tracers) for two flow rates corresponding to the first eight electrodes for a mixer with an overall cycle pattern $[ABCD]_n$, and $\Delta\phi = 2.0 \text{ V}$



When designing such a mixer for experimental study, it remains important to evaluate not only different operating conditions, but overall electrode cycles as well as operating polarities. Figure 4 displays tracer distributions for a mixer with specific parameters $l_e = 500 \mu\text{m}$, $w_g = 50 \mu\text{m}$, and $\Delta\phi = 2.0 \text{ V}$ for two values of $\langle u_z \rangle$. To optimize the mixing efficiency of such a device, it is necessary to test a variety of mixer designs and operating conditions.

3.4 Numerical characterization

The parameters governing the operation of a mixer of this type are $\langle u_z \rangle$, l_e , w_g , $\Delta\phi$, the overall electrode cycle geometry, and the micro-channel substrate(s), i.e., the specific channel surface charge ζ . From the tracer distributions shown in Fig. 4, it appears that the effectiveness of each mixing cycle is related to the total magnitude of helical flow within the primary recirculation region. It is reasonable to assume that higher magnitudes of helical flow will lead to a greater degree of stirring within each recirculation region, thus leading to an increase in mixing efficiency. The magnitude of helical flow within the primary recirculation region can be estimated as the ratio of the average time taken for fluid to migrate down the axial length of an individual electrode and the average time for non-axial transport of fluid across the gap. A mixing effectiveness can therefore be calculated as

$$F = \frac{t_{\parallel}}{t_{\perp}} = \frac{l_e v_{\text{EOF}}}{w_g \langle u_z \rangle} = \frac{l_e \varepsilon_0 \varepsilon_{\zeta} (\Delta\phi)}{w_g^2 \mu \langle u_z \rangle}. \quad (16)$$

As F increases there exists a higher degree of stirring within the primary (and secondary) recirculation regions, which should lead to an increase in mixing efficiency and a decrease in L_{mix} . Because the simulated flow field is a linear superposition of Eq. (4) and the solution to axial flow in a duct, the distribution of tracer particles at the outlet of a mixer (such as that shown in Fig. 1) operating at different conditions will be identical should the two systems possess

the same value of F . Thus for a first generation optimization effort it is only necessary to calculate the extent of mixing at the outlet of each individual electrode while varying the mixing effectiveness F . This provides a direct comparison of overall electrode cycles, and will allow for the optimization of such a mixing device.

Figure 5 displays the conditional entropy S_{1c} as a function of electrode number for several values of F for mixers similar to that in Fig. 1. The mixer shown in Fig. 5a has an overall electrode cycle pattern of $[ABCD]_n$, whereas the mixer shown in Fig. 5b has the overall electrode cycle pattern $[BC]_n$. The individual electrode geometries are shown in Fig. 3, and the values of S_{1c} are computed using $M = 1,000$ equal sized bins. The dotted lines indicate the condition $S_{1c} = 0.9$, above which the cross-sectional planes are classified as well-mixed, i.e., on the order of the width of a bin, $w_b = 3 \mu\text{m}$. The data shown in Fig. 5 follow the same trends for the range of bin numbers $500 < M < 5,000$. It is seen in Fig. 5 that higher magnitudes of F lead to higher rates of mixing, achieving a well mixed condition with fewer electrodes (thus requiring a shorter axial length). For example, for the pattern $[ABCD]_n$ and $F = 80$, only five electrodes are required to reach a value of $S_{1c} = 0.9$, whereas 14 electrodes are required for the same condition when $F = 20$. Figure 5 also includes the simulated mixing profiles for a mixer operated with the polarity reversed (filled symbols $\Delta\phi < 0$). As seen in Fig. 5a, for the pattern $[ABCD]_n$, operation in positive polarity ($\Delta\phi > 0$) results in better overall mixing performance with respect to operation in negative polarity. However, the polarity of the electrodes has little effect on the mixing performance of the $[BC]_n$ electrode pattern. The tracer distributions for the $[BC]_n$ mixer at a effectiveness of $F = 40$ and $F = 10$ may be viewed in Fig. 6. For high values of F , all cases in Fig. 5b resulted in better mixing performance than their counterparts in Fig. 5a; however, for low values of F ($F < 5$) the reverse is true, as the $[ABCD]_n$ electrode cycle pattern displays better mixing performance over its $[BC]_n$ counterpart.

Fig. 5 Comparison of overall cycle pattern **a** $[ABCD]_n$ and **b** $[BC]_n$ using the conditional entropy S_{1c} vs. electrode number for several values of F . The filled symbols indicate mixer operation in reversed polarity ($\Delta\phi < 0$)

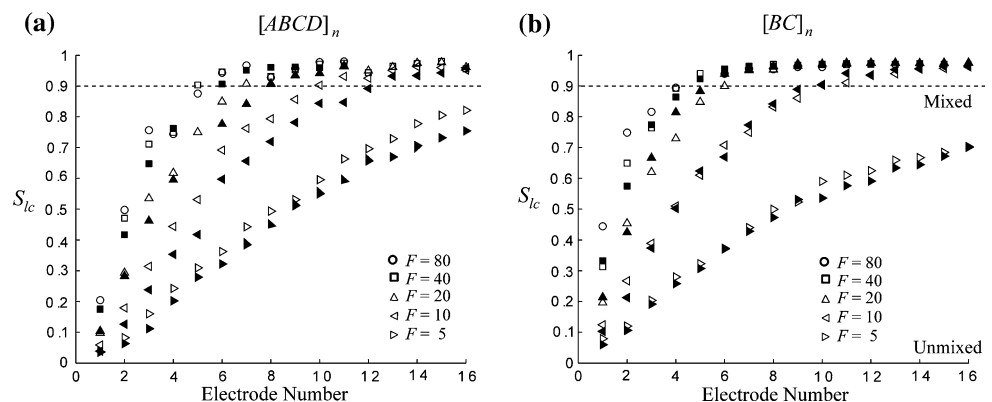
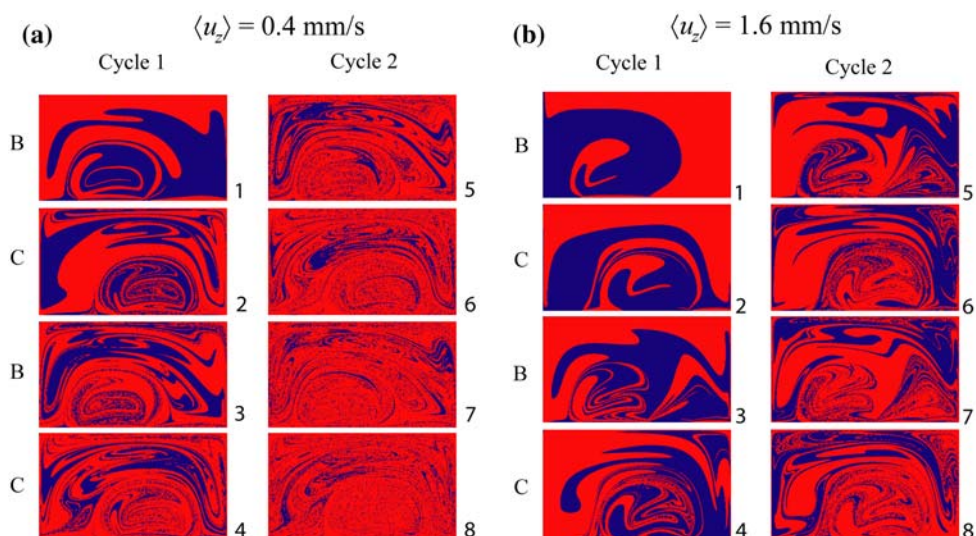


Fig. 6 Tracer distributions (100,000 tracers) for two flow rates corresponding to the first eight electrodes for a mixer with an overall cycle pattern $[BC]_n$, and $\Delta\phi = 2.0$ V



From Fig. 5, it is seen that for a specific electrode number there is a critical value of F , above which a well mixed solution ($S_{lc} > 0.9$) is obtained. Fig. 7a shows the conditional entropy as a function of F along the outlet of the first four electrode cycles corresponding to the pattern $[ABCD]_n$. When the mixing effectiveness is on the order of $F = O(1)$, fluid located just above the electrode gap will complete less than one full recirculation, and only small amounts of stirring occur along the length of each electrode gap. As F increases, there exists more than one recirculation of fluid above the electrode gap, and the extent of mixing rises sharply due to the rapid lamination of fluid within this region. There is a point of diminishing returns for each cycle, however, where subsequent increases in F have little effect on the overall extent of mixing, since the decrease in the striation thickness between two regions of fluid become smaller with every fluid recirculation. In all cases, the addition of more electrode cycles will increase the total extent of mixing at the outlet of a mixer.

Utilizing Eq. (16), the results shown in Fig. 7a can be transformed into data that are commonly acquired in a laboratory experiment. Fig. 7b shows the expected

conditional entropy values as a function of the average linear velocity for a mixer with $l_e = 400$ μm , $h = 60$ μm , $w = 140$ μm , $\Delta\phi = 2.0$ V, and the overall cycle pattern $[ABCD]_n$. As may be expected, the performance of the mixer is somewhat poor at high linear velocities, $\langle u_z \rangle > 6$ mm s^{-1} , while mixing performance increases rapidly as $\langle u_z \rangle$ decreases. For bulk flow rates corresponding to $\langle u_z \rangle < 4$ mm s^{-1} , the extent of mixing of a device can be increased significantly by the addition of multiple electrode cycles. Each electrode cycle shown in Fig. 7b accounts for 1.6 mm of axial channel length; thus, a mixer of this type (operated such that $\langle u_z \rangle < 2$ mm s^{-1}) would be able to provide near complete mixing of a non-diffusive fluid in 6.4 mm of channel length.

4 Experimental results

4.1 Extent of mixing analysis

Based on the above analysis, a four electrode mixer $[ABCD]_3$ (Fig. 8a) was chosen for experimental studies.

Fig. 7 a S_{lc} vs. F measured at the outlet of the first four electrode cycles for a mixer with the overall cycle pattern $[ABCD]_n$. b S_{lc} vs. $\langle u_z \rangle$ for a mixer with $h = 60$ μm , $w = 140$ μm , $l_e = 400$ μm , and $\Delta\phi = 2.0$ V

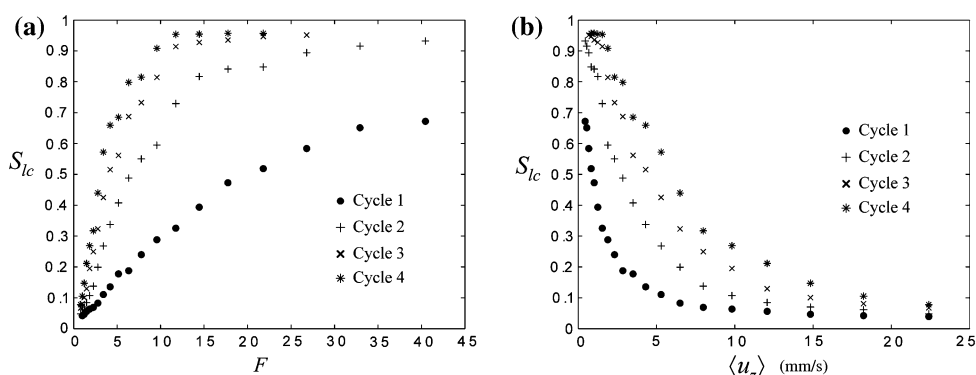
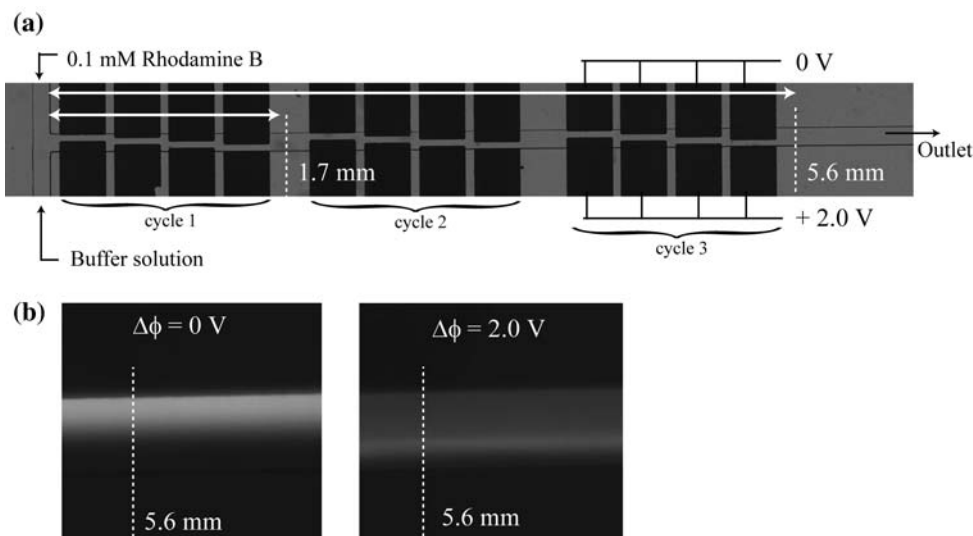


Fig. 8 **a** Picture of experimental mixer used in this study. **b** Fluorescence images regarding $\Delta\phi = 0$ V and $\Delta\phi = 2.0$ V for the experimental mixer operated at $\langle u_z \rangle = 1.6$ mm s⁻¹



The dimensions of the mixer were $w = 140$ μm , $h = 58$ μm , and $l_e = 400$ μm , where the individual electrode cycles matched those shown in Figs. 3 and 7b, with 70 μm spacing between individual electrodes. Mixing experiments were conducted such that two channel inlets containing a buffer solution (TES) were joined in a T-junction immediately upstream of the mixing electrodes, where only one inlet contained a fluorescent dye (0.1 mM rhodamine B). The flow rates of the two solutions were adjusted so that the volumetric flow rate of the buffer solution was twice that of the solution containing the fluorescent dye. The performance of the mixer was evaluated over a range of bulk flow rates, yielding average linear velocities of the dye/buffer solution were within the range $0.5 < \langle u_z \rangle < 12$ mm s⁻¹. After the flow had stabilized, an applied DC potential of $\Delta\phi = 2.0$ V was placed across the electrode pairs. Figure 8b displays top down fluorescence microscopy images of the before ($\Delta\phi = 0$ V) and after ($\Delta\phi = 2.0$ V) states, for $\langle u_z \rangle = 1.6$ mm s⁻¹. Using a series of time averaged images (200 ms), fluorescent line scans across the channel width (averaged over 10 μm) of the mixer situated adjacent to an electrode cycle outlet were used to compute the adjusted extent of mixing (δ_a) via Eq. (13).¹ In these animations, dye initially segregated to one side of the micro-channel is rapidly mixed throughout the channel cross-section upon application of a potential drop across the electrode pairs.

Figure 9 presents δ_a as a function of $\langle u_z \rangle$ for the mixer shown in Fig. 8 operated with $\Delta\phi = 2.0$ V. The intensity values were acquired immediately downstream of the first and third electrode cycles shown in Fig. 8. Mixing was enhanced for all flow rates considered, if only to a small extent at higher bulk flow rates. The adjusted extent of

mixing increases dramatically as $\langle u_z \rangle$ is decreased, experiencing a sharp rise when $\langle u_z \rangle < 3$ mm s⁻¹. As may be expected, δ_a measured after cycle three is greater than all respective values measured after cycle one. It should be noted that, although δ_a provides a good estimate for the overall extent of mixing in the channel cross-sections, it cannot distinguish between a well mixed solution and a solution which is horizontally laminated with fluorescent and non-fluorescent solutions (Munson and Yager 2004). Because top-down microscopic methods were used in this study, these two states are indistinguishable. However, if at any point the channel cross-section were artificially mixed in this manner, one would expect high to low transitions in δ_a values as the effectiveness F of the mixer is increased, e.g., lowering of $\langle u_z \rangle$ shown in Fig. 9. In practice this effect is never observed. Furthermore, the results displayed in Fig. 9 qualitatively agree with those shown in Fig. 7b, created with the numerical model utilizing the same

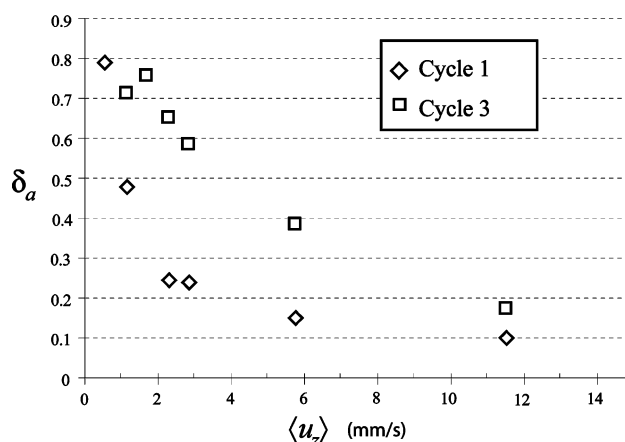


Fig. 9 Adjusted extent of mixing (δ_a) vs. $\langle u_z \rangle$ for the mixer shown in Fig. 8

¹ Animations displaying the on/off operation of the mixing procedure can be found at <http://navier.engr.colostate.edu/eof/>.

geometrical and operating parameters as the experimental device.

4.2 Localized electrolysis

In general, application of a potential across an electrolytic solution will result in electrolysis of water on the surfaces of the integrated electrodes, with acid production localized to the anode and base production on the cathode (Lammertink et al. 2004). Along with localized production of acid and base is the potential for formation of macroscopic O_2 and H_2 bubbles, respectively. Due to the removal of electrolysis products by axial flow, the mixer could be operated continuously ($\Delta\phi < 3.5$ V) for all of the flow rates displayed in Fig. 9 without any apparent formation of gas bubbles. However, at lower bulk flow rates ($\langle u_z \rangle < 0.5$ mm s⁻¹), local acid production can initiate a dramatic loss of the quantum efficiency of rhodamine B, making quantification of the extent of mixing via Eq. (13) difficult at best. Localized regions of low pH can furthermore be detrimental to a mixer of this type through protonation of the micro-channel walls, lowering the overall ζ -potential of the surfaces, and reducing the overall magnitude of EOF within the local regions. For the closed channel recirculating device shown by Lammertink et al. (Lammertink et al. 2004), EOF between two integrated electrodes diminished 30 s after application of a potential difference between the electrodes. Similarly, in the limit $\langle u_z \rangle \rightarrow 0$ the transverse flow mixer in this study experiences the same phenomenon, where the limit of operation is determined by such factors as $\Delta\phi$, ζ , and the concentration of the buffer solution.

To determine where this lower limit of operation might occur, 0.5 μ m diameter fluorescent polymer microspheres (Duke Scientific) were used as a visualization tool. Due to their overall negative surface charge, electrostatic forces dominate in regions of low fluid velocities, and the microspheres attract to the positive electrode. However, fluid velocities within the primary recirculation are high enough to entrap the particles, and helical flow can be viewed directly within this region.² Using these microspheres as a visualization tool, it was found that, for bulk flows corresponding to $\langle u_z \rangle > 0.3$ mm s⁻¹ and $\Delta\phi = 2.0$ V, no loss of transverse EOF over a period of 30 min was observed, during this period the current across the electrode gap remained constant, reaching steady state within several seconds. For fluid velocities close to stagnant ($\langle u_z \rangle \approx 0.05$ mm s⁻¹), the magnitude of transverse

EOF was found to be significantly degraded within 2 min. From the animations, a large degree of fluid interaction within the inter-electrode space is evident for inter-electrode distances of 70 μ m, where there exists transitional helical flow between the staggered electrode gaps. Although the numerical model discussed above neglects this flow, it is clear that along with flow above each electrode gap, this inter-electrode flow can be used to promote a mixing environment. These flow interactions are the focus of future work.

4.3 Operational implications

From Figs. 7 and 9, it is seen that this type of mixer performs best at lower flow rates. The extent of mixing after each electrode cycle at higher bulk flow rates can be increased via an increase of the mixer effectiveness F , which may be accomplished utilizing several strategies. For example, F may be increased directly via an increase in $\Delta\phi$ or l_e . However, these can increase the potential for both macroscopic gas formation and electrochemical interactions, both of which may promote unfavorable side effects. Furthermore, an increase in l_e leads to a mixer that occupies more axial space. The most effective method to increase F is to decrease the size of the electrode gap (w_g), which simultaneously increases the magnitude of the electric field and transverse electroosmotic velocity (constant $\Delta\phi$) between the gap. The decrease in w_g creates a primary recirculation flow profile that exhibits higher fluid velocities yet occupies less space along the channel floor; however, decreasing w_g can result in significant Joule heating effects. Thus, more focus must be placed not only on the overall mixing cycle pattern, but onto the temperature distributions of such a system. Also, the creation of more effective flow patterns may be possible utilizing more electrodes per mixing unit, whereby electrodes can be placed along both the top and bottom walls of a micro-channel. The overall effects of new mixing configurations, along with a minimization of the total electrode surface area in the micro-channel, are the focus of future work.

5 Conclusion

This study demonstrates the capability of a new microfluidic mixing device that combines transverse electroosmotic flow and axial pressure driven flow. The mixer is readily fabricated, and operation requires only a low-voltage power supply and standard methods of fluid delivery. Non-axial flow is produced within the device via transverse electric fields generated by a potential drop across

² Animations of fluorescent microsphere entrapment within the primary recirculation region can be found at <http://navier.engr.colostate.edu/eof/>.

integrated metal electrodes. The degree of mixing over each electrode gap is related to the effectiveness parameter F , which can be directly controlled via geometric parameters (w_g , l_e) or operational conditions ($\langle u_z \rangle$, $\Delta\phi$).

A simplified model combining two-dimensional EOF with uni-directional Poiseuille flow is used to describe the three-dimensional velocity field in the mixer. Utilizing particle tracking of passive tracers, the model is used for an initial survey of the key geometric and operational parameters describing the system. It is shown that the extent of mixing at specified x,y -planes increases as F increases, where these results can be transformed to describe the mixers' performance as a function of $\langle u_z \rangle$. A laboratory device has been fabricated using soft lithographic methods, and the extent of mixing using fluorescent microscopy measured as a function of bulk axial flow. The laboratory mixer displays excellent mixing properties at low values of $\langle u_z \rangle$. Furthermore, the numerical model predictions are in excellent agreement with data acquired from the experimental device. This study presents the first experimental device to utilize combinations of localized transverse electric fields to promote mixing within axial driven flow.

Acknowledgments This work was supported by NIH grant number EB00726.

References

- Altas I, Dym J, Gupta MM, Manohar RP (1998) Multigrid solution of automatically generated high-order discretizations for the biharmonic equation. *SIAM J Sci Comput* 19:1575–1585
- Anderson JL (1989) Colloid Transport by Interfacial Forces. *Annu Rev Fluid Mech* 21:61–99
- Bhattacharya S, Datta A, Berg JM, Gangopadhyay S (2005) Studies on surface wettability of poly(dimethyl) siloxane (PDMS) and glass under oxygen-plasma treatment and correlation with bond strength. *J Microelectromech Syst* 14:590–597
- Biddiss E, Erickson D, Li DQ (2004) Heterogeneous surface charge enhanced micromixing for electrokinetic flows. *Anal Chem* 76:3208–3213
- Camesasca M, Manas-Zloczower I, Kaufman M (2005) Entropic characterization of mixing in microchannels. *J Micromech Microeng* 15:2038–2044
- Camesasca M, Kaufman M, Manas-Zloczower I (2006) Quantifying fluid mixing with the Shannon entropy. *Macromol Theory Simul* 15:595–607
- Cha J, Kim J, Ryu SK, Park J, Jeong Y, Park S, Park S, Kim HC, Chun K (2006) A highly efficient 3D micromixer using soft PDMS bonding. *J Micromech Microeng* 16:1778–1782
- Chang CC, Yang RJ (2004) Computational analysis of electrokinetically driven flow mixing in microchannels with patterned blocks. *J Micromech Microeng* 14:550–558
- Chang CC, Yang RJ (2006) A particle tracking method for analyzing chaotic electroosmotic flow mixing in 3D microchannels with patterned charged surfaces. *J Micromech Microeng* 16:1453–1462
- Chang CC, Yang RJ (2007) Electrokinetic mixing in microfluidic systems. *Microfluidics Nanofluidics* 3:501–525
- Chen H, Meiners JC (2004) Topologic mixing on a microfluidic chip. *Appl Phys Lett* 84:2193–2195
- Dodge A, Jullien MC, Lee YK, Niu X, Okkels F, Tabeling P (2004) An example of a chaotic micromixer: the cross-channel micromixer. *C R Phys* 5:557–563
- Gitlin I, Stroock AD, Whitesides GM, Ajdari A (2003) Pumping based on transverse electrokinetic effects. *Appl Phys Lett* 83:1486–1488
- Hunter RJ (1981) Zeta potential in colloid science. Academic Press, New York
- Jiang F, Drese KS, Hardt S, Kupper M, Schonfeld F (2004) Helical flows and chaotic mixing in curved micro channels. *Aiche J* 50:2297–2305
- Johnson TJ, Locascio LE (2002) Characterization and optimization of slanted well designs for microfluidic mixing under electroosmotic flow. *Lab Chip* 2:135–140
- Kim DS, Lee SW, Kwon TH, Lee SS (2004) A barrier embedded chaotic micromixer. *J Micromech Microeng* 14:798–805
- Lammertink RGH, Schlautmann S, Besselink GAJ, Schasfoort RBM (2004) Recirculation of nanoliter volumes within microfluidic channels. *Anal Chem* 76:3018–3022
- Lee JN, Park C, Whitesides GM (2003) Solvent compatibility of poly(dimethylsiloxane)-based microfluidic devices. *Anal Chem* 75:6544–6554
- Lee CY, Lee GB, Fu LM, Lee KH, Yang RJ (2004) Electrokinetically driven active micro-mixers utilizing zeta potential variation induced by field effect. *J Micromech Microeng* 14:1390–1398
- Leu TS, Ma FC (2005) Novel EHD-pump driven micro mixers. *J Mech* 21:137–144
- Lin H, Storey BD, Oddy MH, Chen CH, Santiago JG (2004) Instability of electrokinetic microchannel flows with conductivity gradients. *Phys Fluids* 16:1922–1935
- Lin JL, Lee KH, Lee GB (2005) Active mixing inside microchannels utilizing dynamic variation of gradient zeta potentials. *Electrophoresis* 26:4605–4615
- McKnight TE, Culbertson CT, Jacobson SC, Ramsey JM (2001) Electroosmotically induced hydraulic pumping with integrated electrodes on microfluidic devices. *Anal Chem* 73:4045–4049
- Meleshko VV (1998) Biharmonic problem in a rectangle. *Appl Sci Res* 58:217–249
- Munson MS, Yager P (2004) Simple quantitative optical method for monitoring the extent of mixing applied to a novel microfluidic mixer. *Analytica Chimica Acta* 507:63–71
- Neils C, Tyree Z, Finlayson B, Folch A (2004) Combinatorial mixing of microfluidic streams. *Lab Chip* 4:342–350
- Niu XZ, Lee YK (2003) Efficient spatial-temporal chaotic mixing in microchannels. *J Micromech Microeng* 13:454–462
- Niu XZ, Liu LY, Wen WJ and Sheng P (2006) Hybrid approach to high-frequency microfluidic mixing. *Phys Rev Lett* 97
- Oddy MH, Santiago JG, Mikkelsen JC (2001) Electrokinetic instability micromixing. *Anal Chem* 73:5822–5832
- Pacheco JR, Chen KP, Hayes MA (2006) Rapid and efficient mixing in a slip-driven three-dimensional flow in a rectangular channel. *Fluid Dyn Res* 38:503–521
- Park J, Shin SM, Huh KY and Kang IS (2005) Application of electrokinetic instability for enhanced mixing in various micro-T-channel geometries. *Phys Fluids* 17
- Qian SZ, Bau HH (2002) A chaotic electroosmotic stirrer. *Anal Chem* 74:3616–3625
- Qian SZ, Bau HH (2005) Theoretical investigation of electro-osmotic flows and chaotic stirring in rectangular cavities. *Appl Math Model* 29:726–753
- Sato H, Ito S, Tajima K, Orimoto N, Shoji S (2005) PDMS microchannels with slanted grooves embedded in three walls to realize efficient spiral flow. *Sens Actuators A Phys* 119:365–371

- Schonfeld F, Hardt S (2004) Simulation of helical flows in microchannels. *Aiche J* 50:771–778
- Selverov KP, Stone HA (2001) Peristaltically driven channel flows with applications toward micromixing. *Physics of Fluids* 13:1837–1859
- Stone ZB, Stone HA (2005) Imaging and quantifying mixing in a model droplet micromixer. *Phys Fluids* 17
- Stone HA, Stroock AD, Ajdari A (2004) Engineering flows in small devices: Microfluidics toward a lab-on-a-chip. *Annu Rev Fluid Mech* 36:381–411
- Stroock AD, Dertinger SK, Whitesides GM, Ajdari A (2002a) Patterning flows using grooved surfaces. *Anal Chem* 74:5306–5312
- Stroock AD, Dertinger SKW, Ajdari A, Mezic I, Stone HA, Whitesides GM (2002b) Chaotic mixer for microchannels. *Science* 295:647–651
- Sundaram N, Tafti DK (2004) Evaluation of microchamber geometries and surface conditions for electrokinetic driven mixing. *Anal Chem* 76:3785–3793
- Sudarsan AP, Ugaz VM (2006) Fluid mixing in planar spiral microchannels. *Lab Chip* 6:74–82
- Suzuki H, Ho CM, Kasagi N (2004) A chaotic mixer for magnetic bead-based micro cell sorter. *J Microelectromech Syst* 13:779–790
- Sze A, Erickson D, Ren LQ, Li DQ (2003) Zeta-potential measurement using the Smoluchowski equation and the slope of the current-time relationship in electroosmotic flow. *J Colloid Interface Sci* 261:402–410
- Therriault D, White SR, Lewis JA (2003) Chaotic mixing in three-dimensional microvascular networks fabricated by direct-write assembly (vol 2, pg 265, 2002). *Nat Mater* 2:347–347
- Vickers JA, Caulum MM, Henry CS (2006) Generation of hydrophilic poly(dimethylsiloxane) for high-performance microchip electrophoresis. *Anal Chem* 78:7446–7452
- West J, Gleeson JP, Alderman J, Collins JK, Berney H (2003) Structuring laminar flows using annular magnetohydrodynamic actuation. *Sens Actuators B Chem* 96:190–199
- Wu HY, Liu CH (2005) A novel electrokinetic micromixer. *Sens Actuators A Phys* 118:107–115
- Xia YN, Whitesides GM (1998) Soft lithography. *Annu Rev Mater Sci* 28:153–184
- Yamaguchi Y, Takagi F, Watari T, Yamashita K, Nakamura H, Shimizu H, Maeda H (2004a) Interface configuration of the two layered laminar flow in a curved microchannel. *Chem Eng J* 101:367–372
- Yamaguchi Y, Takagi F, Yamashita K, Nakamura H, Maeda H, Sotowa K, Kusakabe K, Yamasaki Y, Morooka S (2004b) 3-D simulation and visualization of laminar flow in a microchannel with hair-pin curves. *Aiche J* 50:1530–1535
- Yang JT, Huang KJ, Lin YC (2005) Geometric effects on fluid mixing in passive grooved micromixers. *Lab Chip* 5:1140–1147